Charpy Impact Energy Absorption of 3D Printed Continuous Kevlar Reinforced Composites

Dakota R. Hetrick [a], Seyed Hamid Reza Sanei [a], Omar Ashour [a], Charles E. Bakis [b]

[a] School of Engineering, Penn State Erie, The Behrend College, Erie, PA 16563, USA

[b] Department of Engineering Science and Mechanics, Pennsylvania State University, University Park, PA 16802, USA

Abstract

Additive manufacturing (AM) has been used widely to produce three-dimensional (3D) parts from computer-aided design (CAD) software. Traditional Fused Deposition Modeling (FDM) 3D printed polymer parts lack the necessary strength to be used for functional parts in service. The potential of printing continuous fiber reinforced composites has resulted in parts with better mechanical properties and enhanced performance. Very few studies have investigated the impact energy absorption of continuous fiber reinforced 3D printed composites. The purpose of this work is to investigate the effect of different fiber patterns (unidirectional versus concentric), different stacking patterns (consolidated versus alternating layers), and fiber orientations (0^o, 90^o, 45^o) on the impact energy absorption of 3D printed continuous Kevlar fiber reinforced Onyx composites. Charpy impact testing was used to determine the impact energy absorption of the specimens. It was concluded that alternating the fiber and matrix layers as opposed to consolidating all the fiber layers in the center of the specimen results in lower impact energy absorption. Additionally, the specimens with unidirectional 90° fiber orientation had the lowest impact energy absorption

among the specimens with alternating stacking pattern and those with consolidated ±45° angle-ply fiber orientations had the highest impact energy absorption.

Keywords: 3D Printing; Charpy Impact Testing; Continuous Fiber; Impact Energy; Kevlar Fiber

1. Introduction

Additive manufacturing (AM) is the process of producing three-dimensional (3D) parts from computer-aided design (CAD) files. These files are generated in standard tessellation language (STL) and imported into a software called slicer to be sliced into layers that can be used by a 3D printer. AM has been used in diverse sectors such as automobile industry [1], aerospace applications [2], printing pressure sensors [3–5] and surgical equipment [6]. AM is a broad term that includes many categories: fused deposition modeling (FDM) from polymer filaments, selective laser sintering (SLS) from metal or polymer powders, laminated object manufacturing (LOM) from polymer laminations, and stereolithography (SLA) of a photopolymer liquid [7–10].

FDM is relatively cheap, easy to use, and results in low waste [11–13]. FDM involves generating successive layers of extruded thermoplastic filament to produce 3D geometrical shapes [11]. Traditional and enhanced thermoplastic filament can be used. Traditional thermoplastics include acrylonitrile butadiene styrene (ABS), polylactic acid (PLA), polypropylene (PP), polyethylene (PE) [11,14]. Mechanically enhanced thermoplastics include polyamide (PA or Nylon), polycarbonate (PC), polyetheretherketone (PEEK), polyetherimide (PEI), polyethersulfone (PES), or polyphenylene sulfide (PPS) [11,14].

Polymer parts printed by FDM lack the strength necessary to be used for load-bearing applications. Therefore, their wide use in industrial applications is restricted and the majority of these parts are used as prototypes [11,13,15,16]. Despite the fact that optimizing the FDM printing process

parameters, such as build orientation, layer thickness, or feed rate, and the use of enhanced thermoplastic polymers, have improved the mechanical properties of the produced thermoplastic parts, poor properties of FDM printed parts are attributed to the thermoplastic resin used [11,12,17–21] and porosity inherent in the FDM approach [22,23]. The addition of reinforcements such as fibers, particles, or nanomaterials has enhanced the mechanical properties of 3D printed polymer composites and improved their performance and functionality [24–27]. The potential of printing continuous reinforced fibers into thermoplastic polymers could result in better mechanical properties for demanding applications [24–26]. Markforged, Inc. has developed a semi-industrial grade 3D printer that can print 3D thermoplastic composite parts with a variety of continuous fibers such as glass, Kevlar, and carbon fibers [28]. Studies investigating the mechanical properties of specimen using Markforged printers were summarized in [29,30]. The FDM process involves several parameters and thus many combinations of these parameters. The interactive effects of these parameters on material performance are complex [9,11,12,17,19]. Several studies have investigated the tensile and bending properties of continuous fiber reinforced thermoplastic composites printed by FDM [10,33,34,16,24–26,29–32]. While other research focused on the relationships between FDM process parameters (e.g., build orientation, fiber volume fraction, layer thickness, etc.) and the mechanical properties of continuous fiber reinforced thermoplastic composites [13,31,36]. However, there are few studies on the impact behavior of continuous fiber reinforced thermoplastic composites printed by the FDM process [11,37]. Impact energy absorption of composite materials is an important mechanical property and the lack of it could lead to catastrophic failures during service. Impact damage in composites manifests itself in many forms, such as delamination, fiber breakage, matrix cracking, and fiber and matrix debonding [11,37–40].

Charpy impact testing is often done on injection/compression molded plastics (including chopped fiber filled) to evaluate resistance to impact [41]. Therefore, such testing needs to be applied to 3D printed reinforced composites which can potentially replace molded plastics in various applications. Due to the bending nature of Charpy specimen loading, the build orientation plays an important role in material response. Impact specimens can be printed vertically or horizontally, with the notch up, down or on the side. Caminero et al. [11,37] showed that the maximum impact energy absorption can be achieved by printing the specimen with the notch facing up.

The work reported in this paper is on Charpy impact testing of FDM 3D printed specimens made of Onyx with aramid (Kevlar) as a reinforcement fiber. The specimens were printed on a Markforged® MarkTwo printer horizontally with the notch facing up. The main objective of this study is to investigate the distinctive characteristics of the material when parts are printed with different fiber patterns and orientations and different stacking sequences. Four fiber orientations are considered: 0°, 90°, 45°, and concentric. The 0° orientation is along the length of the Charpy specimen. Concentric fiber begins with the outer geometry of the specimen and infills the outer shape with sequentially smaller rings of printed material. The stacking sequence refers to the order of the layers. This investigation uses alternating and consolidated stacking sequences. The alternating sequence involves alternating single layers of fiber and Onyx while the consolidated stacking sequence alternates groups of consecutive layers of fiber and Onyx. The same overall fiber volume fraction was used in both stacking sequences. The findings of this study will lead to improved material design for impact resistance under bending loads. This paper is organized as follows: Section 2 describes the material and the experimental procedure followed by Section 3 on experiment results and interpretation of data. Section 4 outlines the conclusions of the study and suggests future work.

2. Material and Methods

2.1 3D Printer, Material, and Specimens

The specimens for this work were printed using a Markforged® MarkTwo 3D printer. The printer has the capability to print Nylon printed parts that can be reinforced with a variety of continuous fibers such as glass, Kevlar, and carbon fibers. Markforged® MarkTwo printer has two extruders and uses composite filament fabrication (CFF) technology to print two independent feedstock materials simultaneously. The printer can place concentric rings of fibers as well as unidirectional fiber patterns. Both patterns can be printed independently or simultaneously. For a review of the printer capabilities and limitations, see [29,42].

In this work, a matrix material called Onyx and a binder-infused continuous fiber feedstock were used. The Onyx matrix itself is a composite consisting of Nylon 6 and chopped carbon fiber. Onyx is a proprietary material produced by Markforged, Inc. Therefore, the specifics of the material are unknown except for the basic material properties provided by the manufacturer [28]. The fiber feedstock consists of tow of Kevlar (an aramid fiber produced by DuPont, Inc.) fibers and an undisclosed binding agent that keeps the fibers together throughout the printing process. The Onyx feedstock is 1.75 mm in diameter and the Kevlar feedstock is 0.34 mm in diameter. The mechanical properties of the printed Onyx and Kevlar composites in the longitudinal (printing) direction, along with the mass density of the materials, are presented in Table 1.

Fiber ironing is the printing process that the Markforged® MarkTwo printer uses to fabricate the 3D printed composites. There are two nozzles in the printer head—one to extrude the matrix material (i.e., Onyx) and the other to preheat the fiber feedstock (i.e., Kevlar/binder). The matrix material is extruded in a similar fashion as other FDM printers. The fiber feedstock, on the other hand, is printed differently. The tip of the nozzle has a large flat area, and the heat of the nozzle

melts the binder. Once the fiber feedstock passes through the nozzle, it is flattened out and ironed onto the previous layer with height of 0.1 mm and width of 0.907. This difference in thickness and width of fiber filament makes the print orientation of specimens an important factor. Specimens can be printed flat, horizontally and vertically, as long as they do not exceed the print dimension limitation. The Mark Two can print geometries with volume of 320 (length) by 132 (height) by 154 (width) mm.

The geometry of the specimen is based on the ASTM D6110 standard [41] (see Figure 1). A prototype of the specimen was created before the experiment to evaluate the length of the specimen for a full break. The length of the specimen was modified to be shorter than the recommended length in ASTM D6110 to reduce material consumption and printing time. Dimensions presented in Figure 1 were used for all specimens with different fiber patterns and orientations.

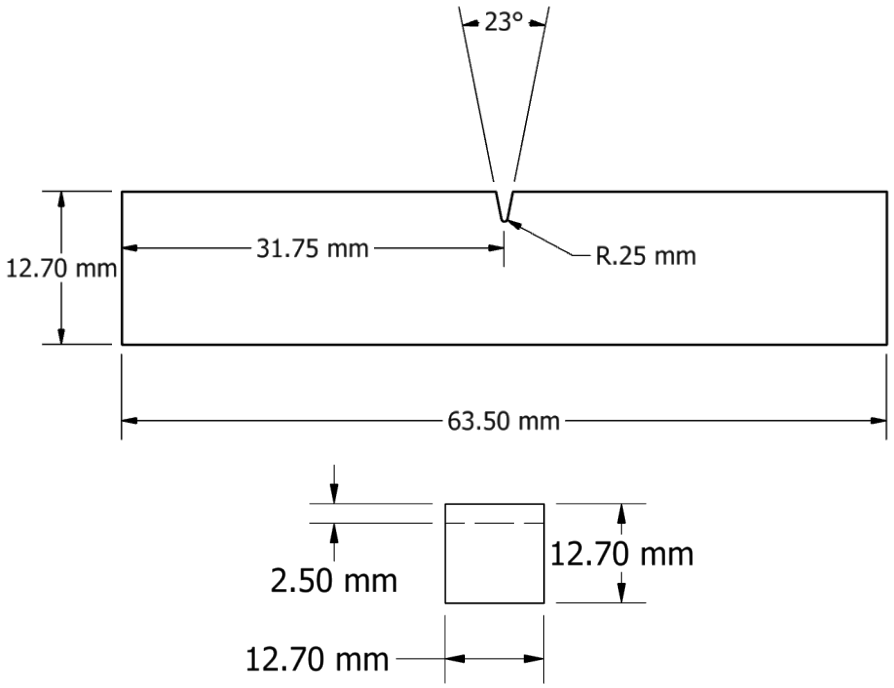

Figure 1. Modified specimen dimensions for Charpy impact testing.

Table 1. Longitudinal mechanical properties and mass density of Onyx and binder-impregnated Kevlar bundle [28]

Properties	Onyx	Kevlar Bundle
Tensile Strength (MPa)	36	610
Tensile Modulus (GPa)	1.4	27
Tensile Break Strain (%)	58	2.7
Flexural Strength (MPa)	81	190
Flexural Modulus (GPa)	2.9	26
Density (g/cm^3)	1.18	1.25

2.2 Printer Parameters, Stacking Sequences, and Fiber Patterns and Orientation

Table 2 shows the FDM print parameters that were used to fabricate the specimens in this study. It has been shown that the print parameters can significantly affect the mechanical properties of the 3D printed parts [43]. Charpy specimens can be printed in four different configurations shown in Figure 2. A horizontal built with the "notch up" configuration was used in this work as it has been shown to have the highest performance [11,37]. In addition, stacking sequences and fiber orientations are key factors that influence the impact resistance of composite parts. In this work, specimens were printed with 127 total layers, as illustrated in Figure 3. All specimens have four layers of floor (bottom layers) and 4 layers of roof (top layers) printed with Onyx at 100 % density. These 8 layers are not included in the stacking sequence designations as they are the same for all configurations. For the remaining 119 layers, 29 layers of Onyx and 30 layers of fibers were printed above and below the midplane of the laminate with symmetry about the midplane and a single layer of Onyx was centered on the midplane. Two types of stacking sequences were implemented: alternating and consolidated. The alternating stacking sequence consists of alternating a single layer of fiber and Onyx, which can be seen in Figure 3 (a). This stacking sequence starts with four floor layers of Onyx then proceeds to alternating fiber and Onyx layers until the part is finished with four roof layers of Onyx. In the alternating stacking sequence, there is always an Onyx layer between two fiber layers. On the other hand, the consolidated stacking sequence groups the 30 layers of fibers together above and below the Onyx midplane followed by 29 layers of Onyx, as shown in Figure 3 (b). Figure 3 also shows examples of the stacking sequence designations. For example, $[(0/X)_{29}/0/\bar{X}]_s$ represents the alternating stacking sequence of 0° fiber layers (0) and Onyx layers (X), where 0° is the long direction of the Charpy specimen, $\bar{X}$ indicates that the single

layer of Onyx is bisected by the midplane of the laminate and subscript *s* indicates symmetry about the midplane.

Table 2. Print parameters used for all specimens

Print Parameter	**Value**
Layer Height (Kevlar and Onyx)	0.1 mm
Infill Pattern	Solid
Infill Density	100%
Use of Brim	Yes
Number of Walls (Surrounding Shell)	2
Number of Roofs (Top Layers)	4
Number of Floors (Bottom Layers)	4
Number of Fiber Layers (In Reinforced Specimens)	60
Number of Onyx Layers	59
Number of Layers (Total)	127

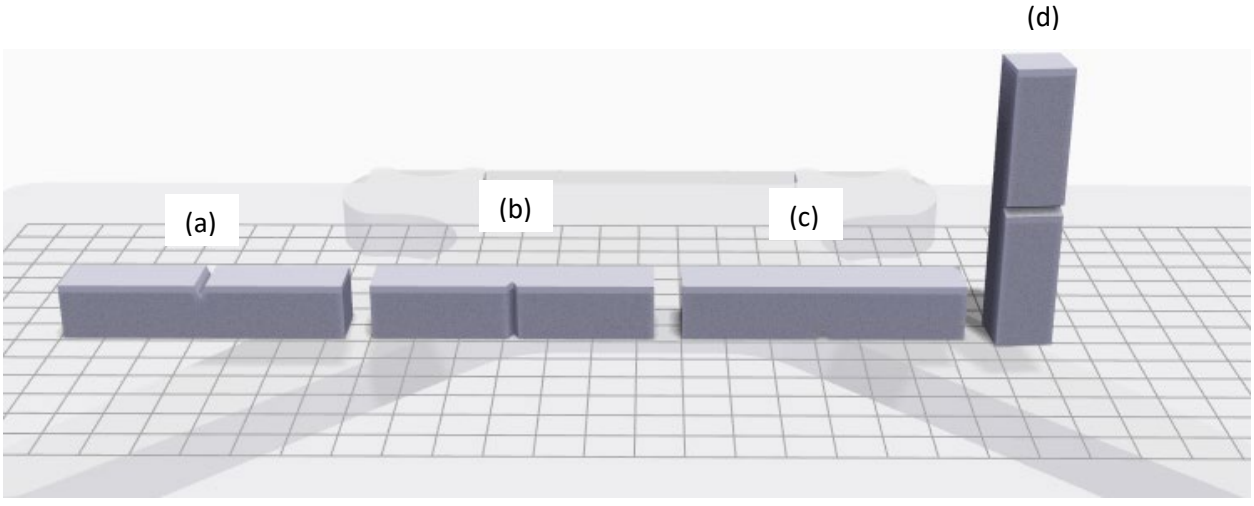

Figure 2. Possible build orientations of Charpy specimens: (a) notch up (used in this investigation), (b) notch on the side, (c) notch down, and (d) vertical

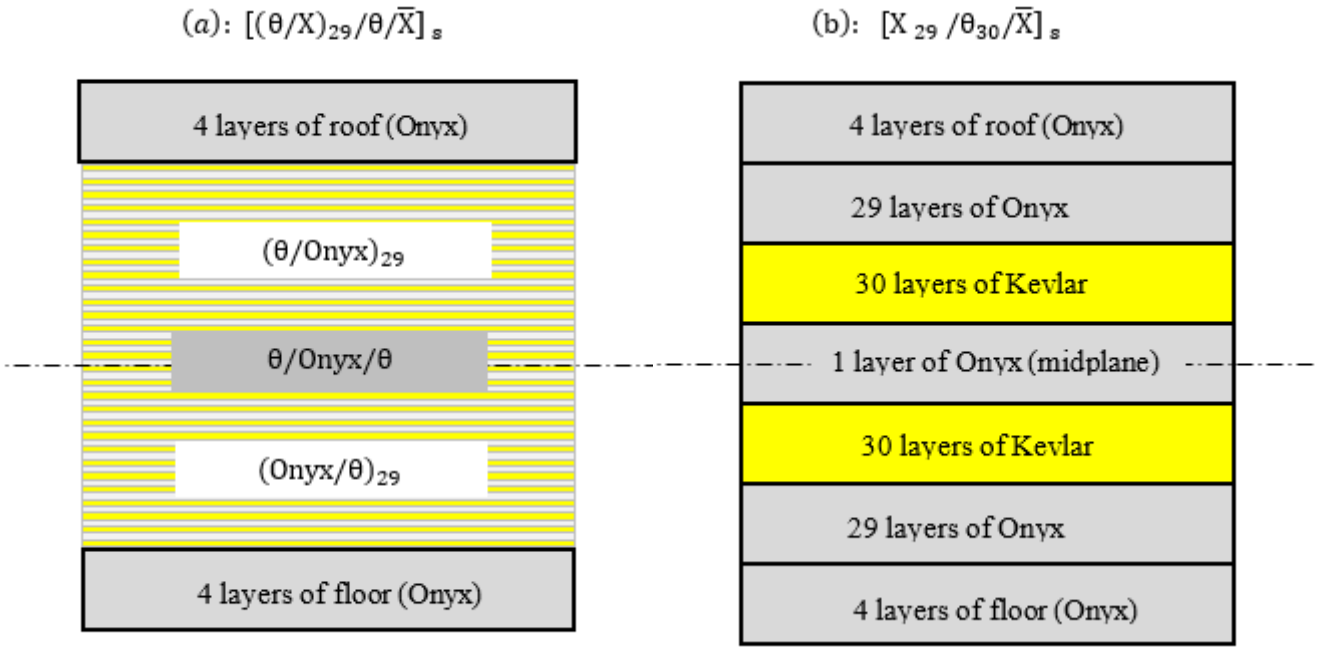

Figure 3. Schematic view of stacking sequence with 127 total layers: (a) alternating stacking sequence, and (b) consolidated stacking sequence

The 0°, 90°, 45°, and concentric fiber patterns are shown in Figure 4 (a), (b), (c), and (d), respectively. The concentric pattern is based on the geometry of the outer wall. The concentric pattern takes the outer wall geometry and offsets the geometry inward towards the center. For specimens with the concentric fiber pattern, five concentric fiber rings were added to the specimen, thus leading to use of the abbreviation "5R" for these specimens in the results. The offsets from one ring to the subsequent rings are not gradual; rather, the printer follows localized 45° offsets to shift its path between rings, as shown in Figure 4 (d). Similar to the unidirectional fiber patterns, the specimens with concentric patterns were printed with consolidated and alternating stacking sequences. Composite properties are driven by the fiber volume fraction [44,45], therefore, all reinforced specimens were printed with the same Kevlar fiber volume fraction of approximately

30%. The fiber volume fraction value is determined by the slicing software (Eiger) as the ratio of reinforcement volume to total volume. This fiber volume fraction does not account for the chopped carbon fibers present in the Onyx material, the binding agent that holds the fiber bundle together and the porosity within and between fiber and Onyx layers. In this work, fiber volume fraction is not altered for different configurations.

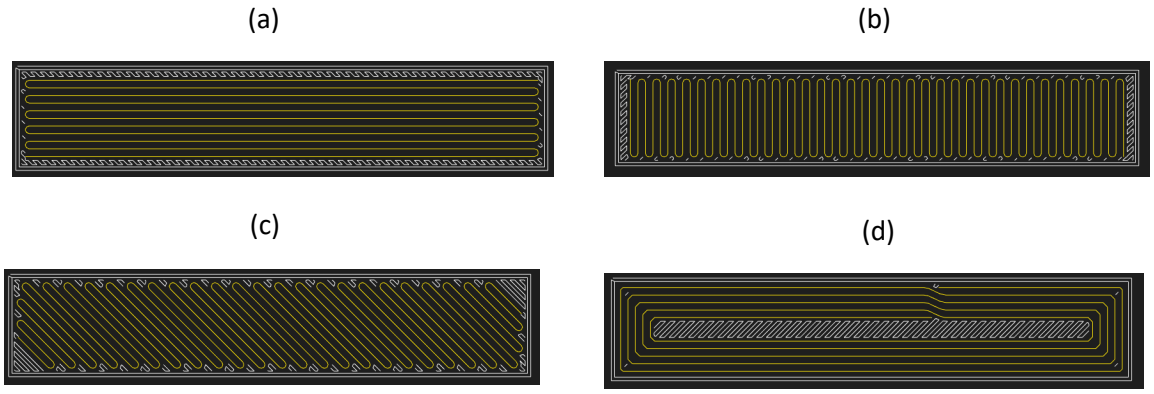

Figure 4. Fiber patterns: (a) 0° fiber, (b) 90° fiber, (c) 45° fiber, and (d) concentric fiber pattern

A set of control specimens were printed as a baseline to be compared to the reinforced specimens. These control specimens were printed with pure Onyx without any continuous fiber reinforcement. The print parameters, notch location and dimensions of the control specimens were identical to the reinforced specimens.

2.3 Mechanical Testing

Four specimens were printed for each stacking sequence and fiber orientation combination. Charpy impact tests were conducted on a single-arm pendulum apparatus as described in ASTM D6110 [29]. Tinius Olsen Model 64 Universal Impact Testing Machine was used which imparts 358 N. m (264

ft.lb) of energy. This apparatus loads the notched specimen in dynamic three-point bending with a span of 41 mm. The machine was electronically calibrated for drag before performing the experiment and the absorbed energy was measured with a digital read-out.

3. Results and Discussion

The average and coefficient of variation (CoV) for the impact energy absorption of all configurations are presented in Table 3 and Figure 5. CoVs were reported only to show the consistency in the obtained results. The authors acknowledge that a larger sample size is needed for in-depth statistical analysis. As expected, the unreinforced control specimen had the lowest energy absorption. The consolidated stacking sequence specimens showed much higher energy absorption than the alternating stacking sequence specimens. Couple of factors could contribute to this phenomenon. First, the binding agent that holds the fiber bundle together during the printing process could produce a stronger adhesion between the fiber layers compared to the adhesion between a fiber layer and an Onyx layer, secondly the placement of adjacent fiber layer could create an air gap between the layers, hence, the specimen would show higher impact resistance. Both of aforementioned hypotheses need to be evaluated by an in-depth X-ray computer topography of internal microstructures of both specimen type.

Table 3. Average impact energy absorption of specimens with different stacking configurations (Symbol *X* denotes an Onyx layer)

Stacking Pattern	**Stacking Sequence**	**Average Energy Absorption in J and (Coef. of Variation)**	**Failure Mode**
Control	$[X_{59}/\bar{X}]_s$	2.0 (4 %)	Split
Consolidated	$[X_{29}/0_{30}/\bar{X}]_s$	20.7 (1%)	Split, In-Plane, Fiber Bridging
Alternating	$[(0/X)_{29}/0/\bar{X}]_s$	10.9 (3%)	Sharp
Consolidated	$[X_{29}/90_{30}/\bar{X}]_s$	22.6 (11%)	Split, In-Plane, Fiber Bridging
Alternating	$[(90/X)_{29}/90/\bar{X}]_s$	3.4 (11%)	Path
Consolidated	$[X_{29}/(0/90)_{15}/\bar{X}]_s$	13.3 (16%)	Split and In-Plane
Alternating	$[(0/X/90/X)_{14}/0/X/90/\bar{X}]_s$	9.2 (8%)	Blunt and Sharp

Consolidated	$[X_{29}/(45/-45)_{15}/\bar{X}]_s$	31.0 (14%)	Split, In-Plane, Fiber Bridging
Alternating	$[(45/X/-45/X)_{14}/45/X/-45/\bar{X}]_s$	13.0 (31%)	Sharp
Concentric Consolidated	$[X_{29}/5R_{30}/\bar{X}]_s$	23.4 (5%)	Split, In-Plane, Fiber Bridging
Concentric Alternating	$[(5R/X)_{29}/5R/\bar{X}]_s$	8.6 (3%)	Sharp

There is large variability in the reinforced specimens compared to control specimens. Concentric fiber patterns showed the lowest variability compared to unidirectional configurations. These variations can be attributed to uncertainty introduced during the printing process such as fiber waviness and void content.

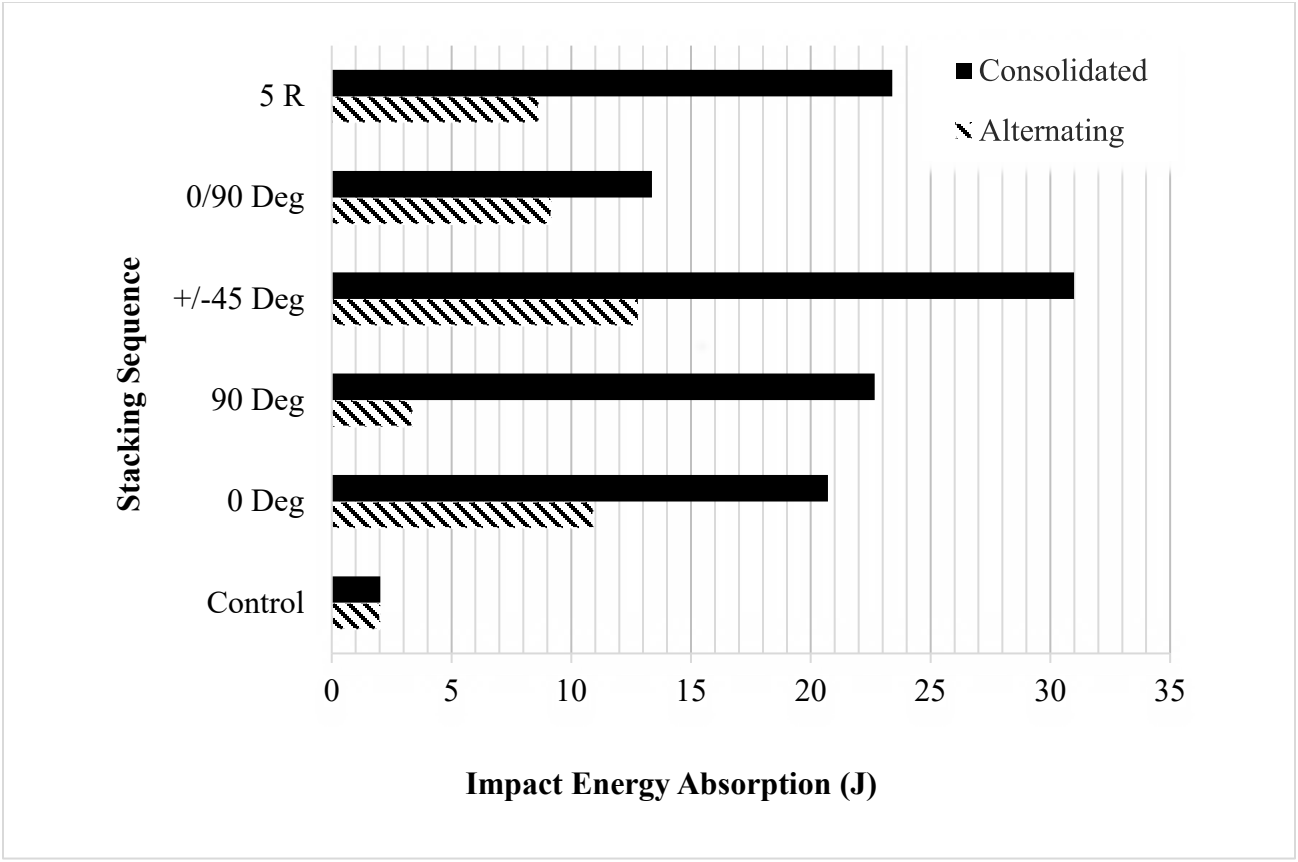

Figure 5. Energy absorption for alternating and consolidated stacking patterns and sequences

3.1 Failure Modes

Table 3 contains a description of the dominant failure mode for each type of specimen. All the control specimens split into two pieces at the notch—similar to how a brittle metal specimen would fracture in the same test scenario. Figure 6 (a) shows an example of such fracture.

3.1.1 Alternating Stacking Sequences

Specimens with alternating stacking sequences showed different failure modes for different fiber orientations. The 0° fiber orientation specimens showed a total fiber failure. It was noted that the matrix layers sheared along the print path to create a triangular protrusion extending outward from one side of the break. This fracture is referred to as sharp fracture and is shown in Figure 6 (b). All

90° specimens failed along the fiber paths. This fracture is referred to as path fracture. Path fracture resulted in a very low energy absorption in the 90° specimens with alternating stacking sequence—only slightly higher than the control specimen. Debonding was the dominant mode of failure and fibers were pulled out unbroken, hence not using their impact absorption capacity consistent with previous observation [40]. The unbroken fibers bridged the fracture path. This phenomenon in a fracture is referred to as fiber bridging and is shown in Figure 6 (c). The 0°/90° specimens behaved more closely to the 0° specimens than to the 90° specimens. There was also a rectangular protrusion extending from the fracture that was not previously observed in the 0° or 90° specimens. This failure mode is referred to as a blunt fracture and shown in Figure 6 (d). Unlike the triangular protrusions from the 0° specimens, these protrusions consist of multiple layers. In the ±45° specimens, fiber bridging was not observed, but there were multiple triangular protrusions extending from the fracture surfaces in each specimen (Figure 6 (b) sharp fracture). Like the 0°/90° specimens, these protrusions consist of multiple layers. Lastly, the concentric ring specimens behaved almost identically to the 0° specimens. The only difference is that there is a patch of matrix material at the center of the concentric ring pattern.

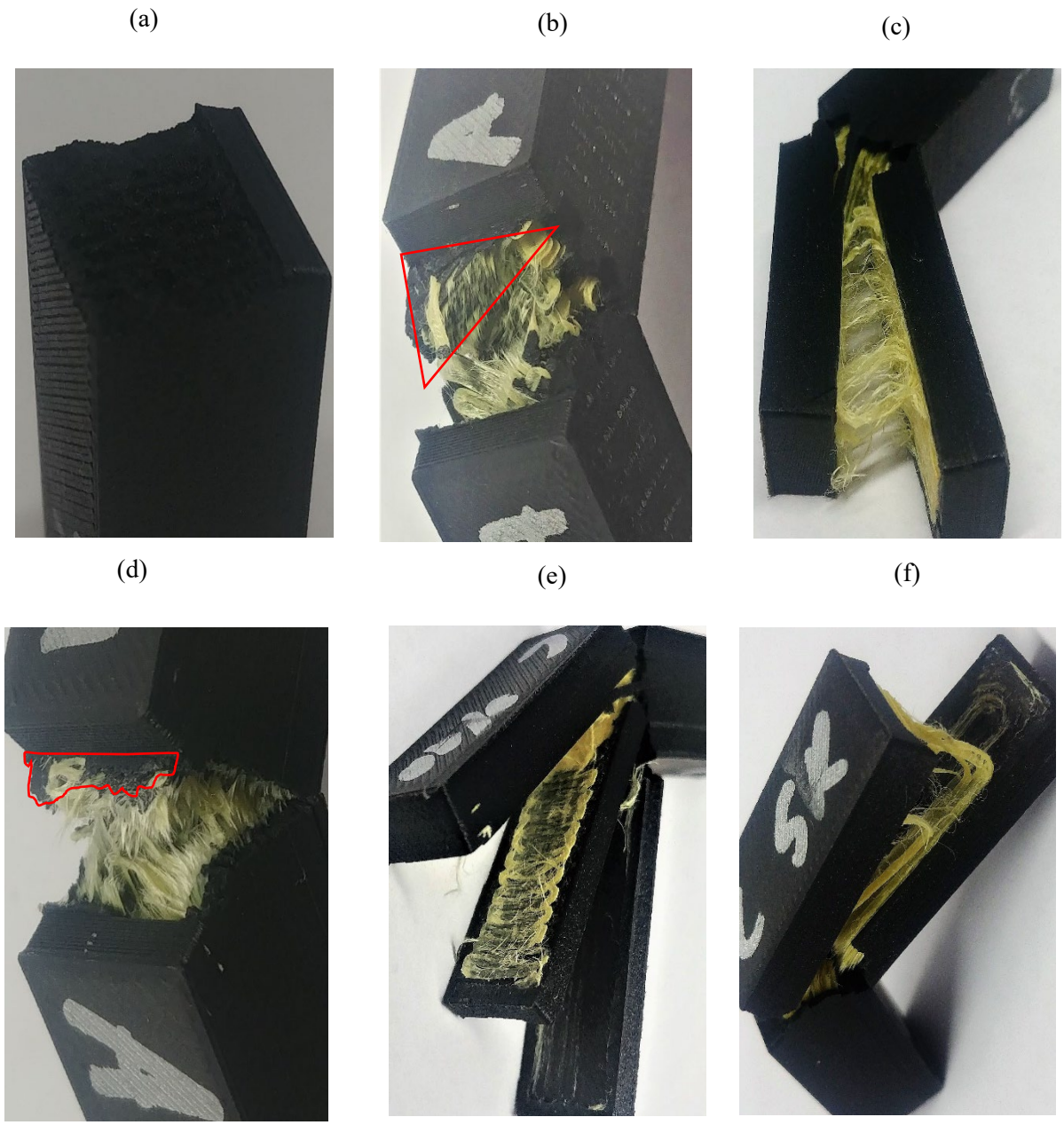

Figure 6. Failure modes observed in impact testing of specimen with different stacking sequence: (a) split, (b) sharp (fracture surface shown by red triangle), (c) fiber bridging, (d) blunt (fracture surface shown by red boundary), (e) in-plane fracture, and (f) concentric fiber peel off

3.1.2. Consolidated Stacking Patterns

Apart from small variations, the failure of all the consolidated stacking sequence specimens was similar to the alternating stacking sequence specimens. During fracture, the fiber block closest to the notch experienced partial fiber failure. The fiber failure stopped at various points after halfway through the fiber block. The fracture path then continued as an in-plane fracture either after or before reaching the matrix layer at the midpoint. Often this in-plane fracture resulted in fiber bridging. In some specimens, there were two in-plane fractures that occurred. A few cases had the outer wall layers of the specimen peeled away from the fibers. There were a few cases in which a small portion of the fracture specimens fragmented off and completely separated itself from the main body of the specimen as shown in Figure 6 (e). For all cases, the consolidated stacking pattern had higher impact energy absorption compared to its alternating counterpart. In the case of concentric fiber patterns, concentric fiber rings are not in contact with one another, making debonding from the adjoining Onyx layer easier. Such peel-off from the Onyx layer can be seen in Figure 6 (f). Despite this dominant mode of failure, specimens with concentric fiber rings with the consolidated stacking sequence had the second highest impact energy absorption.

4. Concluding Remarks and Suggestions

This work investigated the Charpy impact characteristics of 3D printed continuous Kevlar fiber reinforced composites. The specimens were manufactured using FDM technology and a Markforged MarkTwo 3D printer. Among all the stacking sequences and fiber patterns and orientations investigated, specimens with the alternating stacking sequence showed less energy absorption compared to specimens with the consolidated stacking sequence. The $[(90/X)_{29}/90/\bar{X}]_s$ configuration had the lowest energy absorption and the $[X_{29}/(45/-45)_{15}/\bar{X}]_s$ configuration had the highest energy absorption. Six distinct failure modes were observed, i.e., split fracture, in-

plane fracture, path fracture, sharp fracture, fiber bridging and blunt fracture. It was observed that the bond between the alternating fiber and matrix layers is not as strong as the bond between consecutive consolidated fiber layers. Most of failure initiated due to poor bonding between adjacent fiber layers or between fiber and matrix layers. Poor bonding did not allow the full impact absorption capacity of fiber and matrix to be utilized. In future work, close-up inspection of the failure surfaces in a scanning electron microscope (SEM) would be useful to assess the extents of fiber fracture and pullout. X-ray computer topography scan of different specimen types would provide useful insights on evaluating the bond and possible interior gaps between adjacent layers. The effects of varying fiber volume fraction on impact energy absorption should be investigated as well. While not possible with current commercially available printers, other fiber patterns such as sinusoidal paths are worthy of investigation for improved impact energy absorption. Moreover, the impact of void removal should be investigated.

Acknowledgement:

Authors would like to thank the Pennsylvania State University Multi-Campus Research Experience for Undergraduates program for funding this project.

References

[1] Ganesh Sarvankar S, Yewale SN. Additive Manufacturing in Automobile Industry. Int J Res Aeronutical Mech Eng 2019;7:1–10.

[2] Joshi SC, Sheikh AA. 3D printing in aerospace and its long-term sustainability. Virtual Phys Prototyp 2015;10:175–85. https://doi.org/10.1080/17452759.2015.1111519.

[3] Palaniappan V, Masihi S, Panahi M, Maddipatla D, Bose AK, Zhang X, et al. Laser-Assisted Fabrication of a Highly Sensitive and Flexible Micro Pyramid-Structured Pressure Sensor for E-Skin Applications. IEEE Sens J 2020;20:7605–13. https://doi.org/10.1109/JSEN.2020.2989146.

[4] Masihi S, Panahi M, Maddipatla D, Bose AK, Zhang X, Hanson AJ, et al. Development of a Flexible Tunable and Compact Microstrip Antenna via Laser Assisted Patterning of

Copper Film. IEEE Sens J 2020;20:7579–87. https://doi.org/10.1109/JSEN.2020.2987318.

[5] Masihi S, Maddipatla D, Bose AK, Zhang X, Hanson AJ, Palaniappan V, et al. A Novel Printed Fabric Based Porous Capacitive Pressure Sensor For Flexible Electronic Applications. I2019 EEE Sensors, Montreal, QC, Canada: IEEE; 2019, p. 1–4. https://doi.org/10.1109/SENSORS43011.2019.8956672.

[6] Wong JY, Pfahnl AC. 3D printing of surgical instruments for long-duration space missions. Aviat Sp Environ Med 2014;85:758–63. https://doi.org/10.3357/ASEM.3898.2014.

[7] Kotlinski J. Mechanical properties of commercial rapid prototyping materials. Rapid Prototyp J 2014;20:499–510. https://doi.org/10.1108/RPJ-06-2012-0052.

[8] Wang Q, Mitsumura N, Chen Q, Sarkar A, Kurokawa H, Sekiguchi K, et al. Investigation of condensation reaction during phenol liquefaction of waste woody materials. Int J Sustain Dev Plan 2014;9:658–68. https://doi.org/10.2495/SDP-V9-N5-658-668.

[9] Dizon JRC, Espera AH, Chen Q, Advincula RC. Mechanical characterization of 3D-printed polymers. Addit Manuf 2018;20:44–67. https://doi.org/10.1016/j.addma.2017.12.002.

[10] Melenka GW, Cheung BKOO, Schofield JS, Dawson MR, Carey JP. Evaluation and prediction of the tensile properties of continuous fiber-reinforced 3D printed structures. Compos Struct 2016;153:866–75. https://doi.org/10.1016/j.compstruct.2016.07.018.

[11] Caminero MA, Chacón JM, García-Moreno I, Rodríguez GP. Impact damage resistance of 3D printed continuous fibre reinforced thermoplastic composites using fused deposition modelling. Compos Part B Eng 2018;148:93–103. https://doi.org/10.1016/j.compositesb.2018.04.054.

[12] Chacón JM, Caminero MA, García-Plaza E, Núñez PJ. Additive manufacturing of PLA structures using fused deposition modelling: Effect of process parameters on mechanical properties and their optimal selection. Mater Des 2017;124:143–57. https://doi.org/10.1016/j.matdes.2017.03.065.

[13] Dickson AN, Barry JN, McDonnell KA, Dowling DP. Fabrication of continuous carbon, glass and Kevlar fibre reinforced polymer composites using additive manufacturing. Addit Manuf 2017;16:146–52. https://doi.org/10.1016/j.addma.2017.06.004.

[14] Yao SS, Jin FL, Rhee KY, Hui D, Park SJ. Recent advances in carbon-fiber-reinforced thermoplastic composites: A review. Compos Part B Eng 2018;142:241–50. https://doi.org/10.1016/j.compositesb.2017.12.007.

[15] Nakagawa Y, Mori K ichiro, Maeno T. 3D printing of carbon fibre-reinforced plastic parts. Int J Adv Manuf Technol 2017;91:2811–7. https://doi.org/10.1007/s00170-016-9891-7.

[16] Justo J, Távara L, García-Guzmán L, París F. Characterization of 3D printed long fibre reinforced composites. Compos Struct 2018;185:537–48. https://doi.org/10.1016/j.compstruct.2017.11.052.

[17] Song Y, Li Y, Song W, Yee K, Lee KY, Tagarielli VL. Measurements of the mechanical response of unidirectional 3D-printed PLA. Mater Des 2017;123:154–64. https://doi.org/10.1016/j.matdes.2017.03.051.

[18] Wu W, Geng P, Li G, Zhao D, Zhang H, Zhao J. Influence of layer thickness and raster angle on the mechanical properties of 3D-printed PEEK and a comparative mechanical study between PEEK and ABS. Materials (Basel) 2015;8:5834–46. https://doi.org/10.3390/ma8095271.

[19] Zaldivar RJ, Witkin DB, McLouth T, Patel DN, Schmitt K, Nokes JP. Influence of processing and orientation print effects on the mechanical and thermal behavior of 3D-Printed ULTEM ® 9085 Material. Addit Manuf 2017;13:71–80. https://doi.org/10.1016/j.addma.2016.11.007.

[20] Yang C, Tian X, Li D, Cao Y, Zhao F, Shi C. Influence of thermal processing conditions in 3D printing on the crystallinity and mechanical properties of PEEK material. J Mater Process Technol 2017;248:1–7. https://doi.org/10.1016/j.jmatprotec.2017.04.027.

[21] Berretta S, Davies R, Shyng YT, Wang Y, Ghita O. Fused deposition modelling of high temperature polymers: Exploring CNT PEEK composites. Polym Test 2017;63:251–62. https://doi.org/10.1016/j.polymertesting.2017.08.024.

[22] Blok LG, Longana ML, Yu H, Woods BKSS. An investigation into 3D printing of fibre reinforced thermoplastic composites. Addit Manuf 2018;22:176–86. https://doi.org/10.1016/j.addma.2018.04.039.

[23] Ning F, Cong W, Qiu J, Wei J, Wang S. Additive manufacturing of carbon fiber reinforced thermoplastic composites using fused deposition modeling. Compos Part B Eng 2015;80:369–78. https://doi.org/10.1016/j.compositesb.2015.06.013.

[24] Wang X, Jiang M, Zhou Z, Gou J, Hui D. 3D printing of polymer matrix composites: A review and prospective. Compos Part B Eng 2017;110:442–58. https://doi.org/10.1016/j.compositesb.2016.11.034.

[25] Hofstätter T, Pedersen DB, Tosello G, Hansen HN. State-of-the-art of fiber-reinforced polymers in additive manufacturing technologies. J Reinf Plast Compos 2017;36:1061–73. https://doi.org/10.1177/0731684417695648.

[26] Matsuzaki R, Ueda M, Namiki M, Jeong TK, Asahara H, Horiguchi K, et al. Three-dimensional printing of continuous-fiber composites by in-nozzle impregnation. Sci Rep 2016;6:1–7. https://doi.org/10.1038/srep23058.

[27] Sanei SHR, Arndt A, Doles R. Open hole tensile testing of 3D printed continuous carbon fiber reinforced composites. J Compos Mater 2020;54:2687–95. https://doi.org/10.1177/0021998320902510.

[28] Markforged Material Properties Datasheet. Watertwon, MA, USA: 2019.

[29] Sanei SHR, Popescu D. 3D-Printed Carbon Fiber Reinforced Polymer Composites: A Systematic Review. J Compos Sci 2020;4:98. https://doi.org/10.3390/jcs4030098.

[30] Kabir SMF, Mathur K, Seyam AFM. A critical review on 3D printed continuous fiber-

reinforced composites: History, mechanism, materials and properties. Compos Struct 2020;232:111476. https://doi.org/10.1016/j.compstruct.2019.111476.

[31] Parandoush P, Lin D. A review on additive manufacturing of polymer-fiber composites. Compos Struct 2017;182:36–53. https://doi.org/10.1016/j.compstruct.2017.08.088.

[32] Der Klift F Van, Koga Y, Todoroki A, Ueda M, Hirano Y, Matsuzaki R. 3D Printing of Continuous Carbon Fibre Reinforced Thermo-Plastic (CFRTP) Tensile Test Specimens. Open J Compos Mater 2016;06:18–27. https://doi.org/10.4236/ojcm.2016.61003.

[33] Sauer MJ. Evaluation of the mechanical properties of 3D printed carbon fiber composites. MSc thesis. Rapid City, SD, USA: 2018.

[34] Sanei SHR, Lash Z, Servey J, Gardone F, Nikhare CP. Mechanical properties of 3D printed fiber reinforced thermoplastic. ASME Int Mech Eng Congr Expo Proc 2019;12:1–6. https://doi.org/10.1115/IMECE2019-10303.

[35] Hetrick D, Sanei SHR, Bakis CE, Ashour O. Evaluating the Effect of Variable Fiber Content on Mechanical Properties of Additively Manufactured Continuous Carbon Fiber Composites. J Reinf Plast Compos 2020.

[36] Tian X, Liu T, Yang C, Wang Q, Li D. Interface and performance of 3D printed continuous carbon fiber reinforced PLA composites. Compos Part A Appl Sci Manuf 2016;88:198–205. https://doi.org/10.1016/j.compositesa.2016.05.032.

[37] Caminero MA, Rodríguez GP, Muñoz V. Effect of stacking sequence on Charpy impact and flexural damage behavior of composite laminates. Compos Struct 2016;136:345–57. https://doi.org/10.1016/j.compstruct.2015.10.019.

[38] Shi Y, Swait T, Soutis C. Modelling damage evolution in composite laminates subjected to low velocity impact. Compos Struct 2012;94:2902–13. https://doi.org/10.1016/j.compstruct.2012.03.039.

[39] Zhang D, Sun Y, Chen L, Pan N. A comparative study on low-velocity impact response of fabric composite laminates. Mater Des 2013;50:750–6. https://doi.org/10.1016/j.matdes.2013.03.044.

[40] Kabir SMF, Mathur K, Seyam AFM. Impact resistance and failure mechanism of 3D printed continuous fiber-reinforced cellular composites. J Text Inst 2020. https://doi.org/10.1080/00405000.2020.1778223.

[41] ASTM-D6110-18. Standard test method for determining the charpy impact resistance of notched specimens of plastics. West Conshohocken, PA: 2018. https://doi.org/10.1520/D6110-10.1.

[42] Kabir SMF, Mathur K, Seyam A-FM. The Road to Improved Fiber-Reinforced 3D Printing Technology. Technologies 2020;8:51. https://doi.org/10.3390/technologies8040051.

[43] Popescu D, Zapciu A, Amza C, Baciu F, Marinescu R. FDM process parameters influence over the mechanical properties of polymer specimens: A review. Polym Test 2018;69:157–66. https://doi.org/10.1016/j.polymertesting.2018.05.020.

[44] Sanei SHR, Fertig RS. Uncorrelated volume element for stochastic modeling of microstructures based on local fiber volume fraction variation. Compos Sci Technol 2015;117:191–8. https://doi.org/10.1016/j.compscitech.2015.06.010.

[45] Sanei SHR, Barsotti EJ, Leonhardt D, Fertig RS. Characterization, synthetic generation, and statistical equivalence of composite microstructures. J Compos Mater 2017;51:1817–29. https://doi.org/10.1177/0021998316662133.